Virology 417 (2011) 137–146

Contents lists available at ScienceDirect

Virology

journal homepage: www.elsevier.com/locate/yviro

Determinants of the HIV-1 core assembly pathway

Claudia S. López [a,*], Jacob D. Eccles [a], Amelia Still [b], Rachel E. Sloan [a], Robin Lid Barklis [a], Seyram M. Tsagli [a], Eric Barklis [a,*]

[a] Department of Molecular Microbiology and Immunology and Vollum Institute, School of Medicine, Oregon Health & Science University, Portland, OR 97239, USA
[b] Department of Biochemistry, University of Wisconsin, WI, USA

ARTICLE INFO

Article history:
Received 25 March 2011
Accepted 21 May 2011
Available online 14 June 2011

Keywords:
Retrovirus
Microscopy
Core assembly
Nucleation
Gag
Nucleocapsid
RNA

ABSTRACT

Based on structural information, we have analyzed the mechanism of mature HIV-1 core assembly and the contributions of structural elements to the assembly process. Through the use of several *in vitro* assembly assay systems, we have examined details of how capsid (CA) protein helix 1, ß-hairpin and cyclophilin loop elements impact assembly-dependent protein interactions, and we present evidence for a contribution of CA helix 6 to the mature assembly-competent conformation of CA. Additional experiments with mixtures of proteins in assembly reactions provide novel analyses of the mature core assembly mechanism. Our results support a model in which initial assembly products serve as scaffolds for further assembly by converting incoming subunits to assembly proficient conformations, while mutant subunits increase the probability of assembly termination events.

Introduction

The assembly of HIV-1 virus particles is controlled by the 55 kDa polyprotein precursor Gag (PrGag) protein, which is the key structural protein of HIV-1 (Wills and Craven, 1991; Mervis et al., 1988; Wang et al., 1998; Spearman et al., 1994; Reicin et al., 1996; Hermida-Matsumoto and Resh, 1999; Freed, 1998; Ono et al., 2000; Huseby et al., 2005). PrGag is composed of four major domains: matrix (MA), capsid (CA), nucleocapsid (NC), and p6, as well as two small spacer peptides, SP1 (between CA and NC) and SP2 (between NC and p6) (Erickson-Viitanen et al., 1989; Kräusslich et al., 1995; Swanstrom and Wills, 1997; Wiegers et al., 1998; Borsetti et al., 1998; Burniston et al., 1999). MA is the component of PrGag that is responsible for its binding to the plasma membrane (Zhou et al., 1994; Dalton et al., 2007), which helps trigger immature virus particle release (Ono et al., 2000; Li et al., 2007). During or just after immature particle release, proteolytic processing of PrGag results in a conformational change within CA that induces viral morphogenesis. As visualized by electron microscopy (EM), electron dense conical or cylindrical cores composed of about 1000–1500 CA proteins are evident in mature virus particles (Briggs et al., 2003, 2006; Li et al., 2000). Also present within mature cores are NC–viral RNA complexes, and experimental data support a model in which NC binding to RNA helps nucleate core assembly, perhaps by fostering CA dimerization (Dorfman et al., 1993; Gorelick et al., 1993; Berkowitz et al., 1995; Zhang and Barklis, 1997; Zhang et al., 1998; Dawson and Yu, 1998; Cimarelli et al., 2000; Alfadhli et al., 2005; de Marco et al., 2010). Via microscopy analysis of mammalian cells transfected with HIV constructs, it recently has been validated that the viral RNA (vRNA) plays a scaffolding role in HIV-1 assembly, and that complexes of NC–vRNA located at cellular plasma membranes are highly favored sites for assembly (Jouvenet et al., 2009).

Mature HIV-1 CA possesses two independently folded domains; an N-terminal domain (NTD) that is important for formation of CA hexamers, and a C-terminal domain (CTD), that contributes to hexamer formation and also fosters CA dimerization that is essential for particle assembly (Gitti et al., 1996; Momany et al., 1996; Gamble et al., 1997; Berthet-Colominas et al., 1999; Worthylake et al., 1999; Ganser-Pornillos et al., 2007; Pornillos et al., 2009). The CA NTD is composed of seven alpha helices, a cyclophilin (CypA) binding loop between helices 4 and 5, and an N-terminal ß-hairpin loop composed of the first thirteen residues of CA. The interface formed by helices 1 and 2 makes NTD–NTD contacts that are essential for the assembly and stabilization of CA hexamers both *in vivo* and *in vitro*, whereas truncation of the CypA loop fosters the *in vitro* assembly of CA cores (von Schwedler et al., 2003; Douglas et al., 2004; Ganser-Pornillos et al., 2007; Barklis et al., 2009). Other studies have demonstrated that the N-terminal ß-hairpin loop becomes stabilized after processing by a salt bridge formed between residues 1 (proline) and 51 (aspartic acid) and that the presence of the ß-hairpin correlates with mature core assembly (Gamble et al., 1996; Gitti et al., 1996; Gross et al.,

* Corresponding authors at: Department of Molecular Microbiology and Immunology and Vollum Institute, Oregon Health and Science University, 3181 SW Sam Jackson Park Road, Portland, OR 97239, USA. Fax: +1 503 494 6862.
E-mail addresses: lopezcl@ohsu.edu (C.S. López), barklis@ohsu.edu (E. Barklis).

0042-6822/$ – see front matter © 2011 Elsevier Inc. All rights reserved.
doi:10.1016/j.virol.2011.05.011

1998; von Schwedler et al., 1998; Tang et al., 2002; Abdurahman et al., 2007; Monroe et al., 2010). The CA CTD is smaller than the NTD and is composed of a short 3_{10} helix followed by an extended strand and four α-helices (Momany et al., 1996; Gamble et al., 1997; Berthet-Colominas et al., 1999; Worthylake et al., 1999; Alcaraz et al., 2007; Wong et al., 2008; Pornillos et al., 2009; Byeon et al., 2009). The CTD appears to have the capacity to dimerize in several ways (Gamble et al., 1997; Worthylake et al., 1999; Ternois et al., 2005; Ivanov et al., 2007; Byeon et al., 2009), and the dimerization interface depends on residues W184 and M185 (Gamble et al., 1997; Alcaraz et al., 2008; Byeon et al., 2009; Yu et al., 2009). Recent evidence suggests that an interface formed by the CTD dimers of three neighboring CA hexamers might be involved in organizing intermolecular contacts of mature HIV-1 cores (Byeon et al., 2009). In addition to the formation of dimer and hexamer subunits, retroviral CA proteins have the capacity to assemble pentamers, which allow capsid lattices to make closed core structures similar to those of fullerene cones (Ganser et al., 1999 and Li et al., 2000; Pornillos et al., 2011). Based on this type of structure, HIV-1 cores are modeled to be composed of hexameric and pentameric subunits, with seven pentamers located at one end of the core, and five located at the narrow core end (Ganser et al., 1999; Li et al., 2000; Pornillos et al., 2011).

A model for HIV-1 core assembly suggests that three steps may be differentiated: a slow nucleation step, in which the nucleation species is still unknown; a growth step that involves a fast polymerization of the CA protein; and a termination step, which might involve the capping of growing tubes (Barklis et al., 2009). Despite the current structural information of CA hexameric and pentameric forms, it is still not certain how and whether dimers, hexamers and/or pentamers contribute to the nucleation, growth or termination steps during core assembly, and consequently the mechanisms by which HIV-1 CA proteins assemble to form mature cores *in vivo* and *in vitro* are still unknown. One puzzle is how postulated nucleation complexes might serve as templates for rapid polymerization. Also unknown are the factors that dictate sphere versus core or tube assembly, although theoretical studies imply that the monomer orientations of CTDs and NTDs may regulate the curvature of CA lattices (Nguyen et al., 2006; Levandovsky and Zandi, 2009; Krishna et al., 2010).

Several reports have shown that CA cores assembled *in vitro* resemble those observed *in vivo* (Li et al., 2000; Briggs et al., 2003; Ganser-Pornillos et al., 2007; Byeon et al., 2009) affording investigators an avenue to understanding the principles of mature core assembly. *In vitro* assembly reactions using purified HIV-1 CA proteins result in the formation of long tubes, although cones and spheres can be also observed. In this study, we have examined factors that regulate CA assembly using turbidity assays, fluorescence microscopy (FM) and electron microscopy (EM). We have focused our analysis on amino acid residues located on CA NTD helices 1 and 6, and the ß-hairpin and cyclophilin loops, to determine whether perturbations of these residues result in assembly defects that help elucidate the mechanisms of HIV-1 mature core assembly. Using this strategy, we have characterized CA variants that show disparate assembly properties. Replacements of amino acids located at the N- but not C-terminus of helix 1 (I15, R18), and in the hairpin loop (Δ1–16, H12) impaired mature core assembly. Interestingly, amino acid replacements of residues situated in the upper face region of CA contained by NTD helix 6 (L111, W117), which is adjacent to the ß-hairpin and Cyp-A loops, also impacted core formation, indicating that NTD helix 6 is also a key element that regulates CA assembly.

We further determined that one of our helix 1 mutant proteins was capable of acting as a dominant negative with regard to CA tube assembly, suggesting that the equilibrium between tube and sphere formation can be easily skewed towards the termination of core polymerization. Finally, EM experiments using capsid plus nucleocapsid (CANC) proteins and RNA to foster CA oligomerization demonstrate that CA proteins appear to be triggered to switch conformations as they oligomerize, and that assembled proteins facilitate the conversion of new subunits to an assembly competent status. Mechanisms by which nucleation scaffolds thus regulate HIV-1 core assembly are discussed.

Results

Effects of CA mutations on assembly

To help elucidate the mechanism of mature HIV-1 core assembly, we have analyzed factors that regulate the *in vitro* assembly of capsid tubes from HIV-1 CA monomers. We examined the effects of mutations targeted in CA NTD helices 1 and 6, and the β-hairpin and cyclophilin loops. The CA residues on helix 1 targeted for a mutational analysis were isoleucine 15 (I15), proline 17 (P17), arginine 18 (R18), asparagine 21 (N21) and lysine 25 (K25) (Figs. 1A and B). I15 was mutated based on the notion that this residue might be involved in the correct positioning of the β-hairpin loop that is formed during HIV-1 core maturation (Fig. 1B), whereas residues R18, N21 and K25 possess side chains that point toward neighbor CA proteins within hexamers, potentially organizing CA hexameric lattices (Fig. 1A). We examined a ß-hairpin loop deletion protein (Δ1–16; Fig. 1) to extend previous observations (Gross et al., 1998), which suggested that deletion of the first 13 residues of CA was compatible with assembly. We also tested the effects of mutating one residue located within the hairpin loop (H12; Figs. 1C and D), one residue in the CypA loop (M96; Figs. 1C and D), and a deletion of the CypA loop itself. To complement these studies, other residues located in the upper face loop region of CA NTD were targeted. In particular, mutations at helix 6 residues L111 and W117 were generated. These were of interest because helix 6 is adjacent to the biologically important ß-hairpin and CypA loops, and the influence of helix 6 on assembly has as yet not been investigated in detail.

To monitor how mutations affected the kinetics of CA assembly we measured oligomerization of purified WT and mutant CA proteins spectrophotometrically (Lanman et al., 2002; Tang et al., 2003; Douglas et al., 2004; Sticht et al., 2005; del Alamo et al., 2005; Abdurahman et al., 2007; Barklis et al., 2009). The time-dependent formation of light-scattering CA assembly products was monitored for 60 min, and examples of turbidity assay plots are provided in Figs. 2A and B. In Figs. 2C and D maximum absorbance readings from multiple experiments are graphed for all the mutant proteins. As illustrated in Fig. 2A, the P17A mutant CA, as well as the conservative K25R mutant assembled efficiently, whereas the mutant proteins I15D, R18L and, N21L assembled considerably less well than the WT counterpart. As shown in Fig. 2B, one of the helix 6 mutants, L111W, showed higher turbidity values than WT, while the Δ87–97, H12A, and M96A mutants gave roughly WT results. Relative to WT, several helix 1 mutant proteins (I15D, R18H, R18L, R18E, N21L; Figs. 2A and C) gave low turbidity values, indicative of the importance of helix 1 in making protein contacts critical to mature core assembly. We also observed reduced signals from the Δ1–16 ß-hairpin mutant (Figs. 2B and D), consistent with assignment of the ß-hairpin as a regulator of core morphology. Additionally, several helix 6 variants (L111A, L111F, W117A; Figs. 2B and D) demonstrated low to minimal turbidity signals. This was unexpected, because helix 6 previously has not been earmarked as a determinant of core assembly.

Because turbidity assays cannot distinguish between properly assembled tubes and non-specific protein aggregation, we also monitored CA assembly by fluorescence microscopy (FM), using a method that we recently developed for this purpose (Barklis et al., 2009). Briefly, assembly products are adhered to glass coverslips and detected by immunofluorescence such that tubes appear as bright lines against a black background. As an example, in Figs. 3A–D, FM images of the WT, I15D, Δ1–16 and L111W assembly products are shown. Assembled CA tubes were evident as fluorescent (white) lines, particularly with the WT (Fig. 3A) and L111W (Fig. 3D) samples. Such products were rarely seen in the I15D and Δ1–16 proteins (Figs. 3B

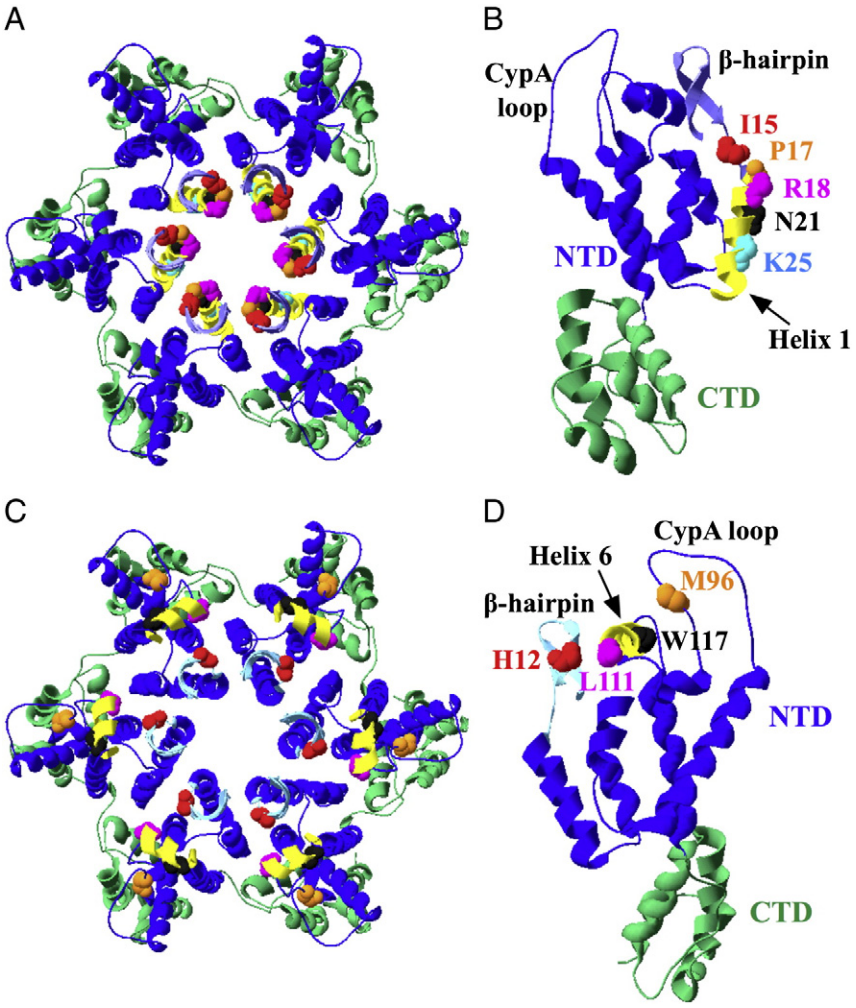

Fig. 1. Locations of HIV-1 CA mutations. The locations of HIV-1 CA helix 1 mutations red (I15), orange (P17), magenta (R18), black (N21) and turquoise (K25) are viewed down the sixfold axis of the CA hexamer (A) and on a monomer model, perpendicularly oriented relative to the hexamer view (B). The locations of HIV-1 CA helix 6 mutations H12 (red), M96 (orange), L111 (magenta), and W117 (black) are viewed down the sixfold axis of the CA hexamer (C) and on a monomer model oriented as in B (D). CA NTDs are colored blue; CTDs are colored green; β-hairpins are colored light blue; and the NTD h1 and h6 helices are colored in yellow. The atomic map derives from PDB 3GV2.

and C), where fluorescent dots, indicative of aggregates or sphere assembly products, were observed. To quantitate results for all the mutants, areas covered by tubes were determined and normalized to WT tube coverage values (Figs. 3E and F). As illustrated, except for Δ87–97 (Fig. 3F), all other variants gave reduced numbers of CA tubes. However, several lysine 25 mutant proteins (K25A, K25R, K25E, K25L) gave at least 25% as many tubes as WT CA (Fig. 3E), as did one conservative helix 6 mutant (L111W), and mutations at M96 in the cyclophilin loop (Fig. 3F). These results are in agreement with turbidity assay results (Fig. 2), and support the notion that alterations in the CypA loop and the C-terminal portion of helix 1 are tolerated for assembly. In contrast, the lowest levels of tube assembly products observed by FM were for N-terminal helix 1 mutant proteins (I15, R18; Fig. 3E), ß-hairpin variants (Δ1–16, H12A; Fig. 3F), and several helix 6 mutant proteins (L111A, L111F, W117A; Fig. 3F). With some exceptions, notably H12A, these results generally correlate with turbidity results, and emphasize the roles of the ß-hairpin and the N-terminus of helix 1 in mature core assembly. They also identify helix 6 as a novel participant in the process.

To complement FM analyses, low magnification EM images of assembly products also were collected. In Figs. 4A–D, examples are illustrated of WT tubes, of short tubes assembled by L111W and of aggregates and spheres formed by I15D and Δ1–16 proteins. As with FM observations, EM results for all proteins were quantified in terms of relative tube assembly efficiencies (normalized percentage area covered by tubes; Figs. 4E and F). Consistent with FM analysis (Fig. 3), mutations that most dramatically reduced tube assembly located to the N-terminal part of helix 1 (I15, R18; Fig. 4E), the ß-hairpin (Δ1–16, H12; Fig. 4E), and helix 6 (L111, W117; Fig. 4F). Thus, in addition to structural elements known to impact mature core formation (ß-hairpin, helix 1), helix 6 also contributes to assembly.

Analysis of assembly inhibition and initiation

As illustrated in Figs. 2–4 above, the I15D replacement in CA NTD helix 1 resulted in the inability of this CA variant protein to adopt an assembly proficient conformation. Indeed, the protein consistently scored among the most assembly-impaired protein variants. To evaluate its effect on assembly competent proteins, we decided to perform coincubations of I15D and the assembly proficient protein Δ87–97, which assembled long tubes as viewed by FM (Figs. 5A–C). For our purposes, the Δ87–97 and I15D proteins were mixed in micromolar ratios of 200/0, 150/0, 100/0, 150/50, 100/100 and 50/150 and allowed to assemble. Incubation products then were subjected to FM analysis (Fig. 5). In the absence of I15D proteins, the Δ87–97 proteins assembled efficiently into tubes at 200, 150 and 100 μM concentrations. In contrast,

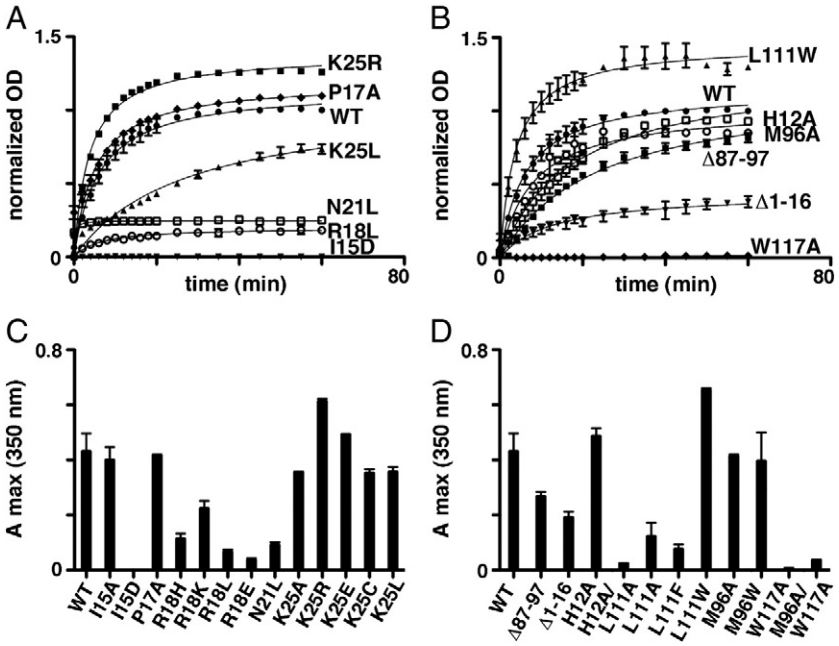

Fig. 2. Effects of mutations on *in vitro* assembly reactions. *In vitro* assembly reactions were performed as described in the Materials and methods section, and assembly was monitored by plotting 350 nm optical density (OD) absorbance values (normalized to those of WT) versus time. In (A), the plots are of WT (black circles), I15D (inverted triangles), P17A (black diamonds), R18L (open circles), N21L (open squares), K25L (triangles), and K25R (black squares). In (B), the plots are of WT (black circles), Δ1–16 (inverted triangles), H12A (open squares), Δ87–97 (black squares) M96A (open circles), L111W (triangles), and W117A (black diamonds). In (C) and (D), the maximum 350 nm OD readings obtained after 60 min incubations for all variants are shown, along with standard deviations. All panels derive from a minimum of at least three independent experiments and show standard deviations, but with some timepoints in panels A–D, the standard deviations are too small to be resolved on the plot.

addition of I15D protein to assembly incubations dramatically reduced the numbers of observed tubes (Figs. 5D–F). Normalized tube coverage values are depicted in Fig. 5G. These data showed that as little as one quarter I15D in an assembly reaction of 200 μM total protein poisoned CA tube assembly. Since 100 μM Δ87–97 by itself assembled tubes efficiently (Figs. 5C and F), the ability of 50 μM I15D CA to inhibit 150 μM Δ87–97 CA from tube formation suggests that one defective CA monomer can impair the activity of more than one assembly competent partner. In an effort to analyze if the I15D and Δ87–97 proteins were homogeneously combined within tubes in the final assembled products, or if there might be a preferential localization of different proteins, we separately tagged the I15D and Δ87–97 proteins with myc and flag epitope tags at their C-termini. Assembly products then were subjected to FM using fluorescently labeled primary antibodies against the myc and flag tags as indicated in the Materials and methods. Interestingly, we observed that the few tubes present in mixed incubations showed an apparent homogeneous distribution of both proteins, suggesting that I15D mutant protein incorporation into tubes did not invariably block tube growth (data not shown).

As a complementary approach to the analysis of CA tube assembly, we have examined the mechanism of tube assembly nucleation. To do so, we took advantage of the fact that HIV-1 CANC proteins can be promoted to assemble tubes under low salt conditions via the addition of RNA. Thus, it is possible to examine how CANC assembly might affect the assembly of CA proteins under conditions in which CA proteins alone don't ordinarily assemble. For the purpose of this study, because CANC plus RNA assembly incubations generated short tubes in our hands, assembly was monitored via EM. As controls, CANC proteins by themselves were incubated in low salt conditions, in the presence of RNA at two different conditions. With these controls, large numbers of tubes were seen at high (30 μM) CANC concentrations (Fig. 6A) while only a few small tubes were observed at low CANC (3 μM) concentrations (Fig. 6B). We then asked whether incubations of RNA plus low concentrations of CANC might be able to nucleate the tube formation of CA proteins under conditions where CA proteins don't normally assemble. To test this, RNA and 3 μM CANC were preincubated 30 min under low salt conditions, and then Δ87–97 CA (40 μM) proteins were added, after which samples were incubated an additional 24 h. Importantly, to avoid CA self-assembly in these samples, the final NaCl concentrations never exceed 25 mM. An example of the products of such an incubation is provided in Fig. 6C. As illustrated, an abundance of small tubes was evident. However, if any of the three incubation components, CA, CANC, or RNA were removed, tube assembly was abolished (Fig. 6D). Thus, the presence of CANC and RNA in low salt conditions triggers HIV-1 CA tube assembly.

We extended these investigations in experiments where CANC proteins in tubes assembled as described above were localized within tubes via immunogold labeling. For these studies, WT CANC proteins and assembly-competent Δ87–97 CA proteins were employed so that the locations in tubes of CANC proteins could be tracked with a primary antibody directed against the CypA loop. As shown in Figs. 7A and B, in incubations where Δ87–97 CA proteins were assembled themselves under high salt conditions, very few gold particles (indicated by black dots) were observed, demonstrating that the Δ87–97 proteins do not bind well to the CypA loop-directed antibody. In contrast, tubes assembled from RNA and high concentrations of WT CANC proteins (Figs. 7C and D) were decorated with gold particles. Tubes assembled under low salt conditions with RNA, low concentrations of WT CANC and high concentrations of Δ87–97 CA also bound gold particles (Figs. 7E–G). It is noteworthy that for incubations containing WT CANC proteins, not all gold particles were tube associated, but this is to be expected, as unassembled and partially assembled CANC proteins will adhere to EM grids and subsequently bind the primary anti-CypA loop antibody and secondary gold-conjugated antibody. For quantitative purposes, to estimate the specificity of antibody binding, we calculated the numbers of gold particles along tube lengths and obtained the following values for the three different incubations: Δ87–97 CA incubations alone, 2.3 particles/micrometer (N = 69 tubes); RNA plus WT CANC, 97.0 particles/micrometer (N = 34); RNA plus WT CANC plus

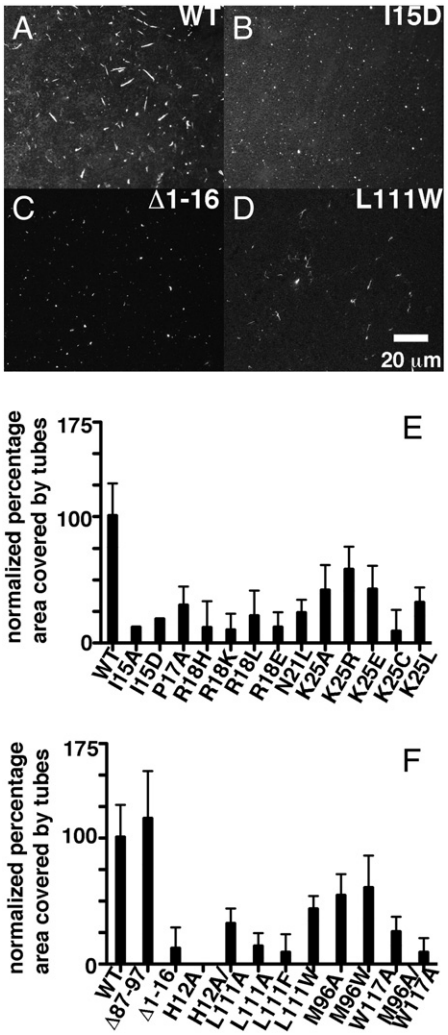

Fig. 3. FM analysis of CA NTD mutant assembly products. WT and CA variant proteins at 80 μM were induced to assemble at 4 °C for 48 h and then processed for visualization by FM. Examples of assembly results for WT (A), I15D (B), Δ1–16 (C), and L111W (D) are shown, where tubes appear as white lines; aggregates and spheres appear as white dots; and the size bar for A–D is as shown in panel D. In panels E and F, tube coverage was calculated from at least five 14,370 μm^2 fields of view of two independent samples for all the CA variants. Results are given as areas covered by tubes, after normalization of results obtained with WT CA.

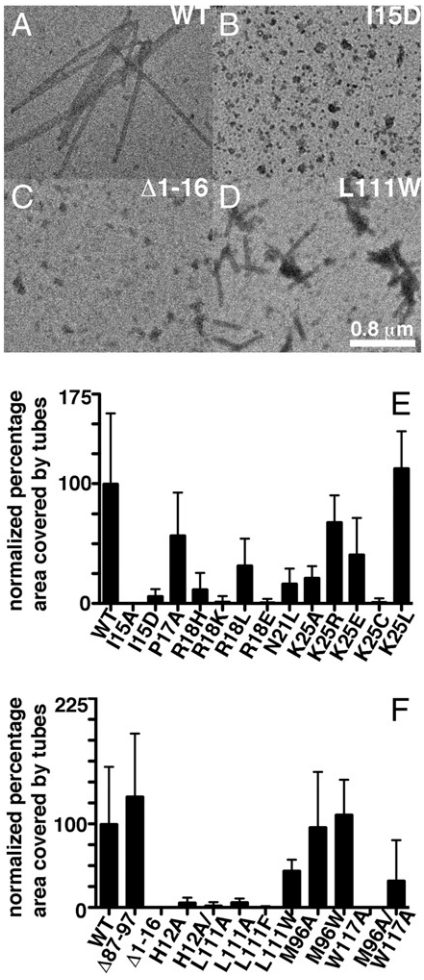

Fig. 4. EM analysis of CA NTD mutant assembly products. WT and CA variant proteins at 80 μM were induced to assemble at 4 °C for 48 h and then processed for viewing by EM after negative staining with uranyl acetate. Examples of assembly results for WT (A), I15D (B), Δ1–16 (C), and L111W (D) are shown, where tubes appear as gray rods; aggregates and spheres appear as black dots or clusters of dots; and the size bar for A–D is as shown in panel D. In panels E and F, tube coverage was calculated from at least six 17.1 μm^2 fields for all CA variants. Results are given as percentage of areas covered by tubes, after normalization of results obtained with WT CA.

Δ87–97 CA, 45.0 particles/micrometer (N = 57). These results indicate that the anti-CypA loop antibody indeed is specific for CANC proteins in these incubations.

Given the specificity of WT CANC protein detection, we next localized CANC proteins in RNA plus CANC tubes (Figs. 7C and D) and in RNA plus CANC plus Δ87–97 CA tubes (Figs. 7E–G). By visual inspection, it appeared that particles on RNA plus CANC tubes were distributed evenly along the lengths of the tubes. In contrast, RNA plus CANC plus Δ87–97 CA tubes showed asymmetric concentrations of particles, usually localized to the end of one tube (Figs. 7E and F, to the left of the arrowheads), but occasionally (two tubes), localized towards the center of the tube (Fig. 7G, between arrowheads). We interpret these images to indicate that short tubes formed from RNA plus CANC proteins can nucleate the assembly of CA proteins either unidirectionally (Figs. 7E and F), or occasionally bidirectionally (Fig. 7G). To quantitate our results, particles were counted along the lengths of multiple tubes from the tube ends that had the highest concentrations of gold particles (defined as the zero ends). In Fig. 7H, the counts are depicted as total particle counts within segments at various distances away from tube zero ends. As shown (Fig. 7H, white bars), tubes composed purely of RNA and CANC proteins demonstrated roughly equal particle counts along their lengths. In contrast, tubes assembled under low salt conditions from RNA, WT CANC and Δ87–97 CA proteins were highly decorated at their zero ends and substantially less decorated at their opposite ends (Fig. 7H, black bars). These results show that CANC proteins localize to single ends of these tubes, and imply that RNA plus CANC assemblies nucleated the assembly of CA proteins. Our results are discussed in further detail below.

Discussion

In this work we have analyzed the mechanism of mature HIV-1 core assembly and the contributions of structural elements to the assembly process. For structural analysis, amino acid modifications of helices 1 and 6, and β-hairpin, and CypA loops residues were evaluated for their effects on mature core assembly. Our results indicate that amino acid changes in helix 1 residues P17 and K25 did not impair assembly (Figs. 2–4). These results were somewhat unexpected because the two residues are highly conserved among HIV CA proteins, and also are located at the helix 1 NTD intra-hexamer interface. In contrast, the other mutations analyzed on helix 1 (I15, R18, N21) and those at the ß-hairpin loop (Δ1–16, H12) showed altered assembly properties (Figs. 2–4).

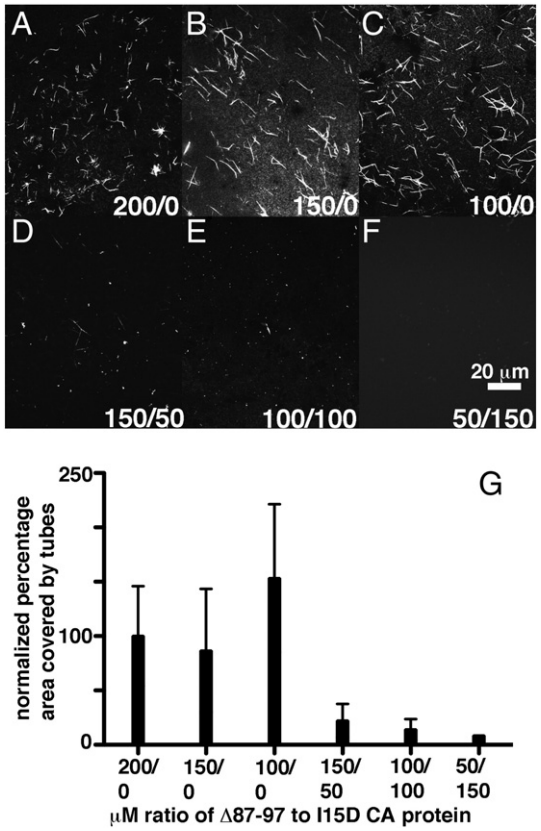

Fig. 5. Effects of I15D proteins on CA assembly. Δ87–97 and I15D proteins at the indicated Δ87–97/I15D concentration ratios were mixed and induced to assemble at 4 °C for 48 h and then processed for visualization by FM. Examples of assembly results for the indicated protein ratios are shown in panels A–F, with the size bar for all these panels in panel F. In panel G, tube coverage was calculated from at least five 14,370 μm^2 fields of view of two independent samples for the indicated mix ratios. Results are given as area covered by tubes, after normalization of results obtained with the 200 μM Δ87–97/0 μM I15D mix.

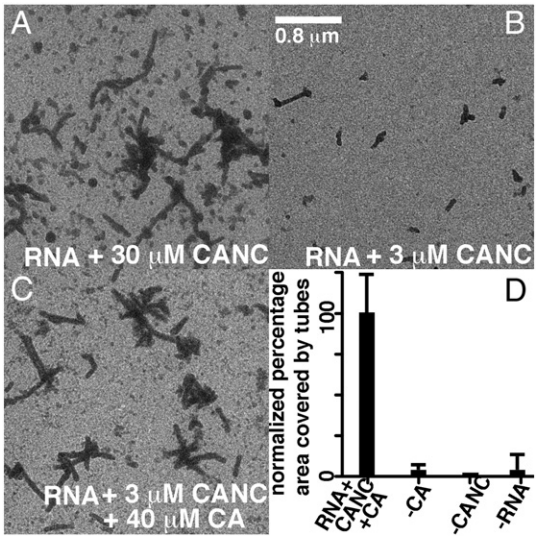

Fig. 6. Assembly of CA and CANC proteins. Panels A–C show EM images of products assembled from RNA (30 μM total nt concentration) and either 30 μM CANC (A), 3 μM CANC (B), or 3 μM CANC plus 40 μM CA protein (C). In panel D, tube coverage was calculated from at least six 17.1 μm^2 fields from samples composed of RNA, 3 μM CANC and 40 μM CA (RNA + CANC + CA); RNA plus 3 μM CANC (− CA); RNA plus 40 μM CA (− CANC); or 3 μM CANC plus 40 μM CA (− RNA). Results are given as percentage of tube area covered by tubes, after normalization of results obtained for the RNA + CANC + CA mix. Note that the average value of the RNA + 3 μM CANC + 40 μM CA mix (corresponding to panel C) was 59% that obtained with the RNA + 30 μM CANC (panel A) incubation.

Since all of these CA variant proteins assembled spherical particles or short tubes, we infer that these proteins are able to nucleate assembly, but that termination occurs prematurely. While previous work suggested that the R18 and N21 residues impact CA assembly, the abnormal assembly observed for the I15 variant may indicate that the side chain of this residue stabilizes or directs the positioning of the β-hairpin loop. Moreover, in contrast to previous results that showed a Δ1–13 deletion of ß-hairpin was compatible with tube assembly (Gross et al., 1998), our data suggest that a deletion of sixteen residues (Δ1–16) impairs mature-type tube formation. One caveat to making distinctions between the assembly properties of the Δ1–13 and Δ1–16 proteins is that the proteins were examined in different studies. However, since the Δ1–16 deletion includes the I15 residue mentioned above, one model of ß-hairpin's role is that it functions to align residues I15 and D51 located in NTD helices 1 and 3 to form NTD–NTD interfaces that are essential for core assembly. Since both the ß-hairpin and CypA loops project away from the centers of cores on CA NTDs, we also were interested in whether mutations at NTD helix 6, situated between these two loops, might affect assembly. Interestingly, we have determined that amino acid replacements of residues L111 and W117 greatly impaired core assembly (Figs. 3 and 4). These data indicate a novel contribution of helix 6 in the control of HIV-1 core morphogenesis and it will be of interest to determine how this regulation occurs.

In addition to evaluating the assembly properties of CA variants, we also have examined how core assembly is terminated and nucleated. As noted above, the I15D protein appears to terminate the growth of capsid tubes. Moreover, when mixed with assembly-competent Δ87–97 proteins very few tubes were observed (Fig. 5) suggesting that one defective CA monomer can impair the activity of more than one assembly competent partner. We envision that I15D proteins may inhibit Δ87–97 tube formation by promoting the capping of tubes resulting in the termination of the polymerization process.

In a second set of mixing experiments, we examined whether short pre-assembled complexes composed of CANC and RNA were able to promote the growth of CA tubes (Fig. 6). Our results indicate that CANC–RNA nucleation complexes acted as seeds for CA tube assembly. To extend this study, we performed immunogold labeling experiments to localize CANC proteins in assembled tubes (Fig. 7). Using this technique, we determined that tubes assembled from RNA, WT CANC, and CA proteins have a preferential distribution of the CANC proteins toward one end, implying that CANC–RNA nucleation complexes indeed nucleated the assembly of CA proteins. Our observations favor a two-step assembly mechanism in which viral RNA plays a nucleating role in HIV-1 mature core assembly. In the first step, nucleation complexes are formed from CANC and RNA; and in a second step, free CA proteins are recruited via specific CA–CA interactions. Our evidence suggests that CA proteins convert to assembly-proficient conformations as they become associated with growing cores. In this regard, it is expected that these CA conformations may be similar to those adopted by CA proteins under assembly-inducing high salt conditions. We also determined that in rare cases (two), nucleation complexes were able to initiate the bidirectional growth of CA tubes (Fig. 7G), indicating that nucleation mostly generated complexes that become capped on one end. We believe that further dissection of these assembly steps will foster the development of antivirals capable of blocking HIV-1 core assembly.

Materials and methods

Recombinant DNA constructs

The parental construct for these studies is pWISP-WTCAH6 (Barklis et al., 2009), which derives from pWISP-98-85 (Li et al., 2000; Ganser-Pornillos et al., 2004), which was kindly provided by Wes Sundquist.

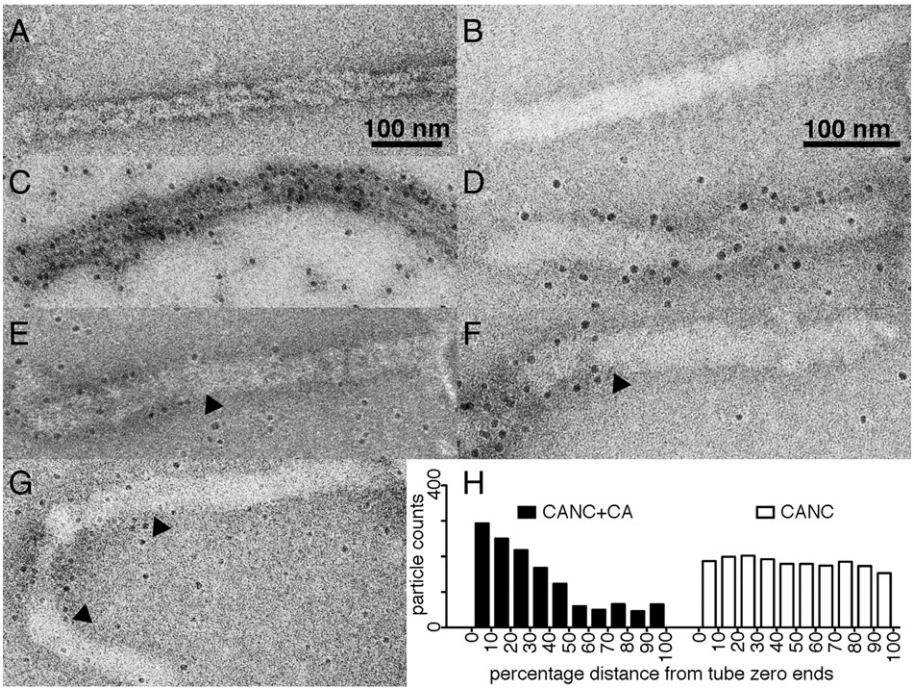

Fig. 7. Immunogold incubations of CA and CANC proteins. Panels A–G show EM images of products assembled from RNA (30 μM total nt concentration) and either 40 μM of Δ87–97 CA proteins (A and B), 30 μM CANC (C and D), or 3 μM CANC plus 40 μM Δ87–97 CA protein (E–G). The primary antibody used for this assay is specific for the CA cyclophilin loop present only in the CANC proteins, and the secondary antibody was gold-conjugated. Gold particles along the tubes can be observed as large black dots. Note that the total numbers of gold particles along tube lengths for the incubations were as follows: Δ87–97 CA alone, 2.3 particles/micrometer (N = 69 tubes); RNA plus WT CANC, 97.0 particles/micrometer (N = 34); RNA plus WT CANC plus Δ87–97 CA, 45.0 particles/micrometer (N = 57). In panel H, particle counts were calculated along tube lengths from 57 assembled tubes composed of RNA plus 3 μM CANC plus 40 μM Δ87–97 CA proteins (black histogram) or 34 tubes of RNA plus 30 μM CANC (white histogram). Note that tube zero ends are defined as the tube ends that had the highest concentrations of gold particles.

This construct expresses C-terminally histidine-tagged (his-tagged) CA proteins; and his-tags, which do not interfere with assembly reactions (Barklis et al., 2009), were not cleaved from the proteins. Mutations were created by standard molecular biology techniques and were sequenced. Mutations are named by the convention where the WT HIV-1 CA residue is listed, followed by the new residue at the mutated position. Nucleotide sequences for point mutations are given below, where underlined nucleotides correspond to the mutated residue, and bold nucleotides represent silent mutations that create or destroy restriction enzyme cleavage sites: H12A, ATG GT**T**GCG CAG GC**G**; I15D, CAG GCC GAC TCA CC**G** C**G**G; I15A, CAG GCC GCT**AGC** CCT; P17A, GC**G** ATA **AGT**GCA**C**G**A** ACT; R18L, GC**G** ATA TCA CCT CTG ACT TTA; R18E, ATA TC**T** CC**G**GAA AC**G** TTA; R18H, GC**G** ATA TCA CCT CAC AC**G** TTA; R18C, GC**G** ATA TC**T** CCG TGC AC**G** TTA; N21L, GC**G** ATA TCA CCT C**G**T AC**G** TTA CTT GCA TGG; K25A, GCA TGG GT**T**GCG GTA GTA GAA GA**A** **GCT**; K25E, GCA TGG GTA GAG GTA GTA GAA GA**A**; K25R, GCA TGG GTA CGC GTA GTA GAA GA**A**; K25L, GCA TGG GTA CTG GTA GTA GAA GA**A**; K25C, GCA TGG GTA TGC GTA GTA GAA GA**A**; M96A, CC**C** GG**G** CAG GCT**C**GA GAA; M96W, CC**C** GGC CAG TGG AGA GAA; L111A, ACT AGT ACC GCC CAG GAA; L111F, ACT AGT ACC TTC CAG GAA; L111W, ACT AGT ACC TGG CAG GAA; W117A, ATA GGC GCC ATG ACA. For deletion mutations, the cyclophilin loop deletion (Δ87–97) corresponds to pWISPΔCycloop-CAH6 (Ganser-Pornillos et al., 2004), while the β-hairpin deletion (Δ1–16) was constructed by eliminating CA codons 1–16. In this case, the nucleotides encoding the CA primary translation product are ATG CC**GC**G**G** AC**C** TTA AAT GCA, where bold nucleotides indicate silent changes to alter restriction sites, the underlined triplet corresponds to codon 17 (proline) and the preceding ATG is the initiator methionine. Previously it has been shown that the initiator methionine of the WT HIV-1 CA protein, which also precedes a proline residue, is removed efficiently in *E. coli* (Li et al., 2000; Ganser-Pornillos et al., 2004), but we have not verified that this is the case with our Δ1–16 construct. In certain experiments, we also have used CA proteins that have been Flag (DYKDDDDK) or Myc (EQKLISEEDL) tagged at their C-termini. The nucleotide sequences at the C-termini of these variants are as follows, where the starting TTG represents the final CA codon, a created NotI restriction site is italicized, the Flag or Myc tag codons are underlined, and the polypeptide nonsense codon is in bold: Flag, TTG CAT CAT CAT CAT CAT CAT *GCG GCC GCG* GAT TAT AAG GAC GAC GAC GAC AAG**TAG**; Myc, TTG CAT CAT CAT CAT CAT CAT *GCG GCC GCG* GAG CAG AAG CTT ATC TCG GAG GAA GAT CTC**TAG**. We also employed WT or Δ87–97 HIV-1 CANC expression constructs that retain the CA coding regions of their namesakes, but express natural HIV-1 CANC proteins with no his tags. These constructs were kindly supplied by Barbie Ganser-Pornillos.

Protein purification

Plasmids were transformed into the *E. coli* strain BL21(DE3)/pLysS (#69451; Novagen) for protein expression and purification, which followed previous procedures (Barklis et al., 2009). Briefly, bacteria were grown in Luria–Bertani (LB) broth supplemented with 0.02% maltose and 10 mM $MgSO_4$ to a 600 nm optical density (OD) of about 0.4, and then induced at 25 °C for 3 h via the addition of 0.5 mM isopropyl-β-D-thiogalactopyranoside (IPTG; Roche #11411446001). In some cases lactose at 1% (w/v) was added instead of IPTG for protein induction. Induced bacteria were collected by centrifugation (Sorvall GSA 5000 rpm, 3000 × *g*, 4 °C) and frozen at −80 °C.

For CA proteins, bacterial pellets were suspended in 10 ml of ice cold 50 mM NaH_2PO_4 pH 7.8, 300 mM NaCl containing 0.5 mg of DNaseI (Roche #10104159001) plus protease inhibitors (15 μg/ml leupeptin, 36 μg/ml egg-white trypsin inhibitor, 36 μg/ml soybean trypsin inhibitor, 30 μg/ml aprotinin, and 1.5 mM phenylmethylsulfonyl fluoride; Sigma). After a 10 min incubation on ice, bacterial suspensions were French-pressed twice, cleared by centrifugation at 23,000 × *g* (Sorvall SS34, 14,000 rpm) for 15 min at 4 °C, and purified by one to two rounds of nickel chelate chromatography (Qiagen Ni-NTA resin, #30210). Non-

specific protein contaminants were washed by increasing the imidazole concentration (10 mM, 25 mM and 50 mM) in wash buffer (50 mM NaH_2PO_4 pH 6, 300 mM NaCl, 10% glycerol), and CA proteins were subsequently eluted in 250 mM imidazole. Purified fractions were subjected to three rounds of buffer exchange by dialysis in buffer 20 mM Tris pH 8.0, 5 mM β-mercaptoethanol (β-Me) for 6 h at 8 °C and protein aliquots were flash frozen on dry ice and stored at −80 °C. Protein identities were assessed by immunoblotting (Barklis et al., 2009), and protein purities of >90% were verified by Coomassie blue staining of samples fractionated by sodium dodecyl sulfate polyacrylamide gel electrophoresis (SDS-PAGE). Previous investigations suggest that the low (<10%) levels of *E. coli* protein contaminants in CA preparations do not interfere with capsid assembly reactions (Ganser-Pornillos et al., 2004; Barklis et al., 2009), but it is possible that minor assembly differences between proteins may be due to minor purity differences. Protein concentrations were determined via 280 nm absorbance readings assuming a molar extinction coefficient of 33,580, and by densitometric comparison of stained SDS-PAGE protein bands versus known standards.

For the purification of CANC proteins, French pressed lysates, prepared as described above, were treated to remove nucleic acids via the addition of 1/167 parts (v/v) of 50% polyethylenimine (Sigma P3134; 0.3% final concentration). Mixtures were incubated on ice for 10 min, and nucleic acid precipitates were removed by 15 min, 4 °C centrifugation at 23,000×*g*. CANC proteins were precipitated from supernatants by the addition of 0.176 g $(NH_4)_2SO_4$ per ml of lysate (30% final concentration), stirring, incubation on wet ice for at least 1 h, and centrifugation as above. Precipitates were suspended in cold loading buffer (25 mM NaH_2PO_4, 150 mM NaCl, pH 7.8) and purified by two rounds of IMAC-Zn (IMAC Sepharose 6 Fast Flow; GE Healthcare 17-0921-67) affinity resin using standard methods (Ganser et al., 1999). Briefly, 1 ml columns were loaded with 200 mM zinc chloride (pH 5.0–5.5), washed with loading buffer, loaded, and washed twice with loading buffer. Fractions were eluted with a series of 1 ml 50 mM sodium acetate, 500 mM NaCl elutions at progressively lower pHs (one time pH 6.0, two times pH 5.0, three times pH 4.0). Elutions were immediately supplemented with 0.05 ml of 1 M Tris pH 9.0 and snap frozen on dry ice powder. Fractions enriched in CANC proteins, as determined by analysis of SDS-PAGE-separated samples, were diluted five to ten times with loading buffer and rerun. The final eluted fractions were then dialyzed against cold 20 mM Tris pH 8.0, 5 mM B-Me, 1 μM $ZnCl_2$ and frozen at −80 °C. Protein identities and purities were assessed as for CA proteins.

In vitro RNA transcription

The nucleic acids used in the *in vitro* CANC assembly reactions were prepared by T7 RNA polymerase transcription (Alfadhli et al., 2009) from SalI (nt 1–4001) or PvuII (nt 1–692) linearized SP64HIV1-4005 plasmids (kindly provided by J.C. Paillart, CNRS-Université de Strasbourg). Briefly, the plasmid digestion products were subjected to phenol/chloroform extraction, after which DNAs were precipitated using 1/10 vol of 3 M sodium acetate pH7.6 and two volumes of ice cold ethanol. DNA pellets were dried and resuspended in TE buffer (10 mM Tris pH7.4, 0.1 mM EDTA). *In vitro* transcription reactions were performed using 2 μl of the T7 polymerase (New England Biolabs M0251S), 10 μl of the supplied 10× buffer, 20 μl of the rNTPs (2.5 mM for each rNTP), 1 μl of RNAsin (Promega 27838911 40 U/μl) and 3 μg of the linearized DNA in a final volume of 100 μl. Mixtures were incubated 1 h at 37 °C, and then 1 μl of the polymerase and 10 μl of the rNTPs were added, and the reactions were incubated for an additional hour at 37 °C. After this incubation step, 1 μl of RNAse-free DNAse (Roche 04716728001) was added to each transcription reaction, and the mixtures were incubated at 37 °C for 10 min prior to the addition of 2 μl RNAsin and 98 μl of DEPC treated water to achieve a final volume of 200 μl. RNAs were purified via two successive phenol/chloroform extractions, and aqueous phases were precipitated by the addition 50 μl of 4 M ammonium acetate and 700 μl ice-cold ethanol. Pelleted precipitates were washed twice with 70% ethanol, suspended in 200 μl DEPC-treated water, and reprecipitated overnight at −80 °C after the addition of 20 μl of 3 M sodium acetate, pH 7.6 and 700 μl ethanol. Final RNA pellets were washed with 200 μl of 70% ethanol, vacuum dried, suspended in 20–30 μl of DEPC-treated water, and stored at −80 °C. RNAs were analyzed by gel electrophoresis. To do so, 2 μl samples and RNA size standards (0.5–10 kb RNA ladder; Invitrogen 15623-200) were mixed with 8 μl of loading buffer (25 mM MOPS, pH 7.0; 6.25 mM sodium acetate, 1.25 mM EDTA, 7.4% formaldehyde, 56.25% formamide, 6.25% glycerol, 0.01% bromophenol blue), heated for 10 min at 70 °C and then run on a 6.67% formaldehyde gel (1–1.5% w/v agarose) using 1× running buffer (20 mM MOPS pH7.0, 5 mM sodium acetate, 1 mM EDTA) in both the gel and electrophoresis apparatus. Samples were electrophoresed 5 h at 100 V, at 4 °C. Following electrophoresis, gels were washed 30 min in 20× SSC (3 M NaCl, 0.3 M sodium citrate), after which RNAs were transferred overnight to nylon membranes (Hybond-N+; GE healthcare RPN303B) by capillary action using 10× SSC. RNAs then were crosslinked by UV treatment (two times 120,000 μJ; UV Stratalinker), after which membranes were stained for 15 min with Methylene blue (300 mM sodium acetate pH 5.2, 5 mM EDTA and 0.03% methylene blue). Stained membranes were washed repeatedly with water until RNA bands were visible. RNA sizes were verified by comparison with standards, and concentrations were calculated by both densitometric comparison with size standards and 260 nm light absorbance assuming an extinction coefficient of 1 OD unit per 40 μg RNA.

CA assembly turbidity assays

HIV-1 CA assembly incubations were performed essentially as described previously (Li et al., 2000; Ganser-Pornillos et al., 2004; Barklis et al., 2009). Turbidity assays were performed at 25 °C using a multiwell plate reader (Molecular devices 190) operating at 350 nm wavelength. Wells were seeded with 20 μl of 50 μM CA, and assembly was initiated by addition of an equal volume of 4 M NaCl. Spectral measurements were taken every 2 min for 20 min and then every 5 min thereafter. For graphing purposes, optical density (OD) values were normalized to those of WT samples performed in parallel. Relative assembly rates (ΔOD/min) were estimated from initial slopes (2 min) of the plots of absorbance versus time. Maximum values were the highest ones obtained during 60 min incubations. All assays were performed at least three independent times, and average values plus standard deviations have been presented.

Fluorescence microscopy

Fluorescence microscopy (FM) assays of CA assembly were performed as described previously (Barklis et al., 2009). Typically, 10 μl reactions included 80 μM protein and 1× FM assembly buffer (50 mM Tris pH 7.0, 1 M NaCl and 5 mM B-Me), and were incubated 48 h at 4 °C. Samples so prepared were processed as described (Barklis et al., 2009), using the following primary antibodies: for CA, media supernatants of cells producing the mouse anti-CA monoclonal antibody Hy183 (kindly provided by Bruce Chesebro, Rocky Mountain Laboratory) were used without dilution; for Flag-tagged proteins, the monoclonal Anti-Flag M2 FITC conjugate (Sigma, F-4049) was used at a dilution of 1:2000; and for Myc-tagged proteins, the Anti-Myc (clone 9E10) Alexa Fluor 555 conjugate (Millipore, 16–263) was used at a dilution of 1:2000. Secondary antibodies used in conjunction with Hy183 were AlexaFluor488- or AlexaFluor544-conjugated goat anti-mouse IgG(H+L) antibodies (Invitrogen), used at dilutions of 1:500 to 1:2000. For assays in which Δ87–97 proteins were Flag-tagged and I15D proteins were Myc-tagged, samples first were subjected to a

complete round of antibody binding and wash steps with one of the antibodies (anti-Flag M2 FITC conjugate) and then were subjected to a second round of labeling using the anti-Myc (clone 9E10) Alexa Fluor555 conjugate. After all antibody binding and wash steps, samples were mounted using Fluoromount-G (SouthernBiotech 0100–01), sealed, and stored at 4 °C prior to viewing. FM imaging was performed on a Zeiss AxioObserver fluorescence microscopes using 20× (LDA-Plan) and 63× (Planapochromat) objectives and a Zeiss filter set 10 (excitation bandpass, 450–490; beamsplitter Fourier transform, 510; emission bandpass, 515–565) for green fluorophores or Zeiss filter set 20 (excitation bandpass, 546/12; beamsplitter Fourier transform, 560; emission bandpass, 575–640) for red fluorophores. Images were collected in gray-scale TIF format using Zeiss Axiovision software. For mixing experiments, we did not observe obvious differences between images of Flag-tagged Δ87–97 proteins and Myc-Tagged I15D proteins, so only images of the Flag-tagged proteins are provided.

Quantitation of FM assembly assay results followed procedures described previously (Barklis et al., 2009). Briefly, gray scale TIF images were opened in Image J, and features were highlighted using the Feature J/FJ Laplacian command with a smoothing step of 1.0. Resulting Laplacian images were thresholded manually using the Image/Adjust/Threshold command, applying threshold values of approximately two standard deviations below the Laplacian image brightness mean. Thresholded images were converted into binary black-white images with the Process/Binary/Make Binary Image J command, which generated images in which tubes appeared as black lines against a white background. For tube coverage tabulation, the Analyze/Analyze Particles command was used, with the size parameter set at 0 to infinity, the circularity parameter set at 0.00 to 1.00, and selecting for the get area fraction output setting, which yields the percentage of the total image area covered by tubes. For each CA variant area fractions were obtained from at least four images, along with images from WT incubations performed in parallel. Results are depicted as areas covered by tubes normalized to the results with WT incubations.

Electron microscopy

Typical assembly incubations for EM analysis employed the conditions indicated above for FM incubations. After the incubations, samples were lifted onto 400-mesh carbon-formvar grids (Ted Pella 01822-F) or 400-mesh ultrathin carbon-over-holey carbon grids (Ted Pella 01824). Samples were lifted onto grids for 3 min, washed for 1 min in water, wicked on filter paper, stained for 45 s in filtered 1.33% uranyl acetate, wicked, and air-dried for 5 min. Samples were viewed at 100 kV on a Philips CM120 TEM, and images were collected as 1024×1024 pixel, 14-bit gray-scale Gatan Digital Micrograph 3 (DM3) files on a Gatan 794 CCD multiscan camera and converted into 8-bit gray-scale TIF images using the program Digital Micrograph 3.4.0.

For quantitation of EM results, at least six 4.136 μm×4.136 μm gray scale TIF images for each variant were analyzed. To do so, image features were highlighted using the Feature J/FJ Laplacian command with a smoothing step of 10 and the zero crossings parameter unselected. Laplacian images were thresholded to low values of 0.10 and maximum high values. For tube coverage tabulation, the Analyze/Analyze Particles command was used with the Analyze/Set Measurements area and Feret's diameter options highlighted. The Analyze Particles command was called with size and circularity arguments as for FM analysis, and results (including particle ID numbers, particle areas, and Feret diameters) were saved in table format. Tube candidates then were excluded if they did not meet the criteria of having a Feret's diameter of at least 50, and a $(\text{Feret})^2/(\text{area})$ value of at least 4. After performing these qualification steps, total areas covered by tubes were summed and divided by total areas to obtain area fractions covered by tubes. Results are depicted as areas covered by tubes normalized to the results with WT incubations.

CANC assembly incubations

CANC assembly incubations were performed in the presence or absence of RNA and/or CA proteins as indicated in the figure legends. For standard reactions, 3 or 30 μM WT or Δ87–97 CANC proteins were incubated in 10 or 20 μl reactions with HIV 1–4001 or 1–692 *in vitro* transcribed RNAs (30 μM total nt concentration) at 4 °C for 24 h in 20 mM Tris pH 7.0, 5 mM B-Me, 1 μM $ZnCl_2$. In reactions containing CA proteins, the CANC and RNA components were pre-incubated 30 min at 4 °C prior to addition of WT or Δ87–97 CA. Incomplete reactions in which individual CANC, CA, or RNA components were excluded, also were performed. For analysis, incubation products were processed for EM as described above.

Immunogold incubations

The CANC samples processed for immunogold incubations were assembled as mentioned above. For this assay we utilized nickel grids (Ted Pella 01800N-F) treated with poly-L-lysine (0.01% solution, Sigma P4707) for 2 min at room temperature. Samples were lifted onto these grids for 3 min, wicked on filter paper and incubated for 30 min at 4 °C in 4% (w/v) paraformaldehyde, 2.5% glutaraldehyde (v/v) prepared in 1× phosphate saline buffer pH 7.4 (PBS). After this step, the grids were wicked and washed in 1× PBS for 1 min. Grids were blocked then in 1× PBS containing 0.5% BSA (PBS + BSA) for 30 min at room temperature, then incubated with the primary antibody raised against the cyclophilin loop (Advanced Biotechnologies Inc., 13-102-100) at 1/500 dilution in PBS + BSA for another 30 min. The grids were then wicked, washed three times for 1 min in PBS + BSA, wicked again and incubated for 30 min at room temperature in 10 nm gold conjugated Goat anti mouse IgG (H + L) (AH) (Ted Pella, 15751) 1/10 dilution in PBS + BSA. After this incubation step the grids were washed three times for 1 min in PBS + BSA, followed by a single wash in filtered water. The grids were wicked on filter paper and stained for 45 s in filtered 1.33% uranyl acetate, wicked, and air-dried for 5 min.

For analysis of immunogold samples, tubes were viewed and tube lengths were measured on Image J. Gold particles along the length of each tube were counted and measured. For comparison of tube labeling, total particle counts per unit length were tabulated. For comparison of the locations of gold particles along tube lengths, one end of each tube was defined as its zero end, and corresponded to the one with more gold particle labeling in the terminal 10% of the tube. Once zero ends were assigned, distances of each gold particle from zero ends were tabulated. To compile results for multiple tubes in each data set, distances of gold particles from zero ends were converted from absolute distances to normalized percentage distances, in which the absolute distance of each particle from its zero end was divided by the length of the tube. For each data set, the numbers of particles along tube length intervals were summed to generate histograms of gold particle counts versus normalized distances from tube zero ends.

Acknowledgments

This research was supported by National Institutes of Health grants GM060170 and AI071798 to E.B and by the Collins Medical Trust to C.S.L. We also appreciate the help and support of Ayna Alfadhli, Henry McNett and Colleen Noviello.

References

Abdurahman, S., Youssefi, M., Höglund, S., Vahlne, A., 2007. Characterization of the invariable residue 51 mutations of human immunodeficiency virus type 1 capsid protein on *in vitro* CA assembly and infectivity. Retrovirology 4, 69–80.

Alcaraz, L.A., del Alamo, M., Barrera, F.N., Mateu, M.G., Neira, J.L., 2007. Flexibility in HIV-1 assembly subunits: solution structure of the monomeric C-terminal domain of the capsid protein. Biophys. J. 93 (4), 1264–1276.

Alcaraz, L.A., Del Alamo, M., Mateu, M.G., Neira, J.L., 2008. Structural mobility of the monomeric C-terminal domain of the HIV-1 capsid protein. FEBS J. 275 (13), 3299–3311.
Alfadhli, A., Dhenub, T.C., Still, A., Barklis, E., 2005. Analysis of human immunodeficiency virus type 1 Gag dimerization-induced assembly. J. Virol. 79 (23), 14498–14506.
Alfadhli, A., Still, A., Barklis, E., 2009. Analysis of human immunodeficiency virus type 1 matrix binding to membranes and nucleic acids. J. Virol. (23), 12196–12203.
Barklis, E., Alfadhli, A., McQuaw, C., Yalamuri, S., Still, A., Barklis, R.L., Kukull, B., López, C.S., 2009. Characterization of the *in vitro* HIV-1 capsid assembly pathway. J. Mol. Biol. 387 (2), 376–389 27.
Berkowitz, R.D., Ohagen, A., Höglund, S., Goff, S.P., 1995. Retroviral nucleocapsid domains mediate the specific recognition of genomic viral RNAs by chimeric Gag polyproteins during RNA packaging *in vivo*. J. Virol. 69 (10), 6445–6456.
Berthet-Colominas, C., Monaco, S., Novelli, A., Sibai, G., Mallet, F., Cusack, S., 1999. Head-to-tail dimers and interdomain flexibility revealed by the crystal structure of HIV-1 capsid protein (p24) complexed with a monoclonal antibody Fab. EMBO J. 18 (5), 1124–1136.
Borsetti, A., Öhagen, Å., Göttlinger, H.G., 1998. The C-terminal half of the human immunodeficiency virus type 1 Gag precursor is sufficient for efficient particle assembly. J. Virol. 72, 9313–9317.
Briggs, J.A.G., Wilk, T., Welker, R., Kräusslich, H.G., Fuller, S.D., 2003. Structural organization of authentic, mature HIV-1 virions and cores. EMBO J. 22, 1707–1715.
Briggs, J.A.G., Grunewald, K., Glass, B., Forster, F., Kräusslich, H.G., Fuller, S., 2006. The mechanism of HIV-1 core assembly: insights from three-dimensional reconstructions of authentic virions. Structure 14, 15–20.
Burniston, M.T., Cimarelli, A., Colgan, J., Curtis, S.P., Luban, J., 1999. Human immunodeficiency virus type 1 Gag polyprotein multimerization requires the nucleocapsid domain and RNA and is promoted by the capsid–dimer interface and the basic region of matrix protein. J. Virol. 73 (10), 8527–8540.
Byeon, I.J., Meng, X., Jung, J., Zhao, G., Yang, R., Ahn, J., Shi, J., Concel, J., Aiken, C., Zhang, P., Gronenborn, A.M., 2009. Structural convergence between Cryo-EM and NMR reveals intersubunit interactions critical for HIV-1 capsid function. Cell 139 (4), 780–790 13.
Cimarelli, A., Sandin, S., Höglund, S., Luban, J., 2000. Basic residues in human immunodeficiency virus type 1 nucleocapsid promote virion assembly via interaction with RNA. J. Virol. 74, 3046–3057.
Dalton, A.K., Ako-Adjei, D., Murray, P.S., Murray, D., Vogt, V.M., 2007. Electrostatic interactions drive membrane association of the human immunodeficiency virus type 1 Gag MA domain. J. Virol. 81 (12), 6434–6445.
Dawson, L., Yu, X.F., 1998. The role of nucleocapsid of HIV-1 in virus assembly. Virology 251 (1), 141–157.
de Marco, A., Davey, N.E., Ulbrich, P., Phillips, J.M., Lux, V., Riches, J.D., Fuzik, T., Ruml, T., Kräusslich, H.G., Vogt, V.M., Briggs, J.A., 2010. Conserved and variable features of Gag structure and arrangement in immature retrovirus particles. J. Virol. 84 (22), 11729–11736.
del Alamo, M., Rivas, G., Mateu, M.G., 2005. Effect of macromolecular crowding agents on human immunodeficiency virus type 1 capsid protein assembly *in vitro*. J. Virol. 79 (22), 14271–14281.
Dorfman, T., Luban, J., Goff, S.P., Haseltine, W.A., Gottlinger, H.G., 1993. Mapping of functionally important residues of a cysteine-histidine box in the human immunodeficiency virus type 1 nucleocapsid protein. J. Virol. 67 (10), 6159–6169.
Douglas, C.C., Thomas, D., Lanman, J., Prevelige Jr., P.E., 2004. Investigation of N-terminal domain charged residues on the assembly and stability of HIV-1 CA. Biochemistry 43 (32), 10435–10441 17.
Erickson-Viitanen, S., Manfredi, J., Viitanen, P., Tribe, D.E., Tritch, R., Hutchison III, C.A., Loeb, D.D., Swanstrom, R., 1989. Cleavage of HIV-1 gag polyprotein synthesized *in vitro*: sequential cleavage by the viral protease. AIDS Res. Hum. Retroviruses 5 (6), 577–591.
Freed, E.O., 1998. HIV-1 Gag proteins: diverse functions in the virus life cycle. Virology 251 (1), 1–15.
Gamble, T.R., Vajdos, F.F., Yoo, S., Worthylake, D.K., Houseweart, M., Sundquist, W.I., Hill, C.P., 1996. Crystal structure of human cyclophilin A bound to the amino-terminal domain of HIV-1 capsid. Cell 87 (7), 1285–1294.
Gamble, T., Yoo, S., Vajdos, F., von Schwedler, U., Worthylake, D., Wang, H., McCutcheon, J., Sundquist, W., Hill, C., 1997. Structure of the carboxy-terminal dimerization domain of the HIV-1 capsid protein. Science 278, 849–853.
Ganser, B.K., Li, S., Klishko, V.Y., Finch, J.T., Sundquist, W.I., 1999. Assembly and analysis of conical models for the HIV-1 core. Science 283, 80–83.
Ganser-Pornillos, B.K., von Schwedler, U.K., Stray, K.M., Aiken, C., Sundquist, W.I., 2004. Assembly properties of the human immunodeficiency virus type 1 CA protein. J. Virol. 78, 2545–2552.
Ganser-Pornillos, B.K., Cheng, A., Yeager, M., 2007. Structure of full-length HIV-1 CA: a model for the mature capsid lattice. Cell 131 (1), 70–79 5.
Gitti, R.K., Lee, B.M., Walker, J., Summers, M.F., Yoo, S., Sundquist, W.I., 1996. Structure of the amino-terminal core domain of the HIV-1 capsid protein. Science 273 (5272), 231–235.
Gorelick, R.J., Chabot, D.J., Rein, A., Henderson, L.E., Arthur, L.O., 1993. The two zinc fingers in the human immunodeficiency virus type 1 nucleocapsid protein are not functionally equivalent. J. Virol. 67 (7), 4027–4036.
Gross, I., Hohenberg, H., Huckhagel, C., Kräusslich, H.G., 1998. N-terminal extension of human immunodeficiency virus capsid protein converts the *in vitro* assembly phenotype from tubular to spherical particles. J. Virol. 72, 4798–4810.
Hermida-Matsumoto, L., Resh, M.D., 1999. Human immunodeficiency virus type 1 protease triggers a myristoyl switch that modulates membrane binding of Pr55 (gag) and p17MA. J. Virol. 73 (3), 1902–1908.
Huseby, D., Barklis, R.L., Alfadhli, A., Barklis, E., 2005. Assembly of human immunodeficiency virus precursor Gag proteins. J. Biol. Chem. 280, 17664–17670.
Ivanov, D., Tsodikov, O.V., Kasanov, J., Ellenberger, T., Wagner, G., Collins, T., 2007. Domain-swapped dimerization of the HIV-1 capsid C-terminal domain. Proc. Natl Acad. Sci. U. S. A. 104 (11), 4353–4358.
Jouvenet, N., Simon, S.M., Bieniasz, P.D., 2009. Imaging the interaction of HIV-1 genomes and Gag during assembly of individual viral particles. Proc. Natl Acad. Sci. U. S. A. 106 (45), 19114–19119.
Kräusslich, H.G., Fäcke, M., Heuser, A.M., Konvalinka, J., Zentgraf, H., 1995. The spacer peptide between human immunodeficiency virus capsid and nucleocapsid proteins is essential for ordered assembly and viral infectivity. J. Virol. 69, 3407–3419.
Krishna, V., Ayton, G.S., Voth, G.A., 2010. Role of protein interactions in defining HIV-1 viral capsid shape and stability: a coarse-grained analysis. Biophys. J. 98 (1), 18–26.
Lanman, J., Sexton, J., Sakalian, M., Prevelige Jr., P.E., 2002. Kinetic analysis of the role of intersubunit interactions in human immunodeficiency virus type 1 capsid protein assembly in vitro. J. Virol. 76 (14), 6900–6908.
Levandovsky, A., Zandi, R., 2009. Nonequilibirum assembly, retroviruses, and conical structures. Phys. Rev. Lett. 102 (19), 198102.
Li, S., Hill, C.P., Sundquist, W.I., Finch, J.T., 2000. Image reconstructions of helical assemblies of the HIV-1 CA protein. Nature 407, 409–413.
Li, H., Dou, J., Ding, L., Spearman, P., 2007. Myristoylation is required for human immunodeficiency virus type 1 Gag–Gag multimerization in mammalian cells. J. Virol. 81 (23), 12899–12910.
Mervis, R.J., Ahmad, N., Lillehoj, E.P., Raum, M.G., Salazar, F.H., Chan, H.W., Venkatesan, S., 1988. The gag gene products of human immunodeficiency virus type 1: alignment within the gag open reading frame, identification of posttranslational modifications, and evidence for alternative gag precursors. J. Virol. 62 (11), 3993–4002.
Momany, C., Kovari, L.C., Prongay, A.J., Keller, W., Gitti, R.K., Lee, B.M., Gorbalenya, A.E., Tong, L., McClure, J., Ehrlich, L.S., Summers, M.F., Carter, C., 1996. Crystal structure of dimeric HIV-1 capsid protein. Nat. Struct. Biol. 3 (9), 763–770.
Monroe, E.B., Kang, S., Kyere, S.K., Li, R., Prevelige Jr., P.E., 2010. Hydrogen/deuterium exchange analysis of HIV-1 capsid assembly and maturation. Structure 18 (11), 1483–1491.
Nguyen, T.T., Bruinsma, R.F., Gelbart, W.M., 2006. Continuum theory of retroviral capsids. Phys. Rev. Lett. 96 (7), 078102.
Ono, A., Demirov, D., Freed, E.O., 2000. Relationship between human immunodeficiency virus type 1 Gag multimerization and membrane binding. J. Virol. 74, 5142–5150.
Pornillos, O., Ganser-Pornillos, B.K., Kelly, B.N., Hua, Y., Whitby, F.G., Stout, C.D., Sundquist, W.I., Hill, C.P., Yeager, M., 2009. X-ray structures of the hexameric building block of the HIV capsid. Cell 137 (7), 1282–1292.
Pornillos, O., Ganser-Pornillos, B.K., Yeager, M., 2011. Atomic-level modelling of the HIV capsid. Nature 469 (7330), 424–427 20.
Reicin, A.S., Öhagen, Å., Yin, L., Höglund, S., Goff, S.P., 1996. The role of Gag in human immunodeficiency virus type 1 virion morphogenesis and early steps of the viral life cycle. J. Virol. 70, 8645–8652.
Spearman, P., Wang, J.J., Vander Heyden, N., Ratner, L., 1994. Identification of human immunodeficiency virus type 1 Gag protein domains essential to membrane binding and particle assembly. J. Virol. 68, 3232–3242.
Sticht, J., Humbert, M., Findlow, S., Bodem, J., Müller, B., Dietrich, U., Werner, J., Kräusslich, H.G., 2005. A peptide inhibitor of HIV-1 assembly *in vitro*. Nat. Struct. Mol. Biol. 12 (8), 671–677.
Swanstrom, R., Wills, J.W., 1997. Retroviruses. In: Coffin, J.M., Hughes, S.H., Varmus, H.E. (Eds.), Cold Spring Harbor Laboratory Press, Cold Spring Harbor, NY, pp. 263–334.
Tang, C., Ndassa, Y., Summers, M.F., 2002. Structure of the N-terminal 283-residue fragment of the immature HIV-1 Gag polyprotein. Nat. Struct. Biol. 9 (7), 537–543.
Tang, C., Loeliger, E., Kinde, I., Kyere, S., Mayo, K., Barklis, E., Sun, Y., Huang, M., Summers, M.F., 2003. Antiviral inhibition of the HIV-1 capsid protein. J. Mol. Biol. 327 (5), 1013–1020.
Ternois, F., Sticht, J., Duquerroy, S., Kräusslich, H.G., Rey, F.A., 2005. The HIV-1 capsid protein C-terminal domain in complex with a virus assembly inhibitor. Nat. Struct. Mol. Biol. 12 (8), 678–682.
von Schwedler, U., Stemmler, T., Klishko, V., Li, S., Albertine, K., Davis, D., Sundquist, W., 1998. Proteolytic refolding of the HIV-1 capsid protein amino-terminus facilitates viral core assembly. EMBO J. 17, 1555–1568.
von Schwedler, U.K., Stray, K.M., Garrus, J.E., Sundquist, W.I., 2003. Functional surfaces of the human immunodeficiency virus type 1 capsid protein. J. Virol. 77, 5439–5450.
Wang, C.T., Lai, H.Y., Li, J.J., 1998. Analysis of minimal human immunodeficiency virus type 1 gag coding sequences capable of virus-like particle assembly and release. J. Virol. 72 (10), 7950–7959.
Wiegers, K., Rutter, G., Kottler, H., Tessmer, U., Hohenberg, H., Krausslich, H.G., 1998. Sequential steps in human immunodeficiency virus particle maturation revealed by alterations of individual Gag polyprotein cleavage sites. J. Virol. 72 (4), 2846–2854.
Wills, J.W., Craven, R.C., 1991. Form, function, and use of retroviral gag proteins. AIDS 5, 639–654.
Wong, H.C., Shin, R., Krishna, N.R., 2008. Solution structure of a double mutant of the carboxy-terminal dimerization domain of the HIV-1 capsid protein. Biochemistry 47 (8), 2289–2297.
Worthylake, D.K., Wang, H., Yoo, S., Sundquist, W.I., Hill, C.P., 1999. Structures of the HIV-1 capsid protein dimerization domain at 2.6 A resolution. Acta Crystallogr. D Biol. Crystallogr. 55 (Pt. 1), 85–92.
Yu, X., Wang, Q., Yang, J.C., Buch, I., Tsai, C.J., Ma, B., Cheng, S.Z., Nussinov, R., Zheng, J., 2009. Mutational analysis and allosteric effects in the HIV-1 capsid protein carboxyl-terminal dimerization domain. Biomacromolecules 10 (2), 390–399.
Zhang, Y., Barklis, E., 1997. Effects of nucleocapsid mutations on human immunodeficiency virus assembly and RNA encapsidation. J. Virol. 71 (9), 6765–6776.
Zhang, Y., Qian, H., Love, Z., Barklis, E., 1998. Analysis of the assembly function of the human immunodeficiency virus type 1 gag protein nucleocapsid domain. J. Virol. 72 (3), 1782–1789.
Zhou, W., Parent, L.J., Wills, J.W., Resh, M.D., 1994. Identification of a membrane-binding domain within the amino-terminal region of human immunodeficiency virus type 1 Gag protein which interacts with acidic phospholipids. J. Virol. 68 (4), 2556–2569.